

## **SEPARATION OF ISOCHROMATICS AND ISOCLINICS PHASEMAPS FOR THE PHOTOELASTIC TECHNIQUE WITH USE PHASE SHIFTING AND A LARGE NUMBER OF HIGH PRECISION IMAGES**

**Cristina Almeida Magalhães<sup>1)</sup>, Perrin Smith Neto<sup>2)</sup>, Pedro Américo Almeida Magalhães Júnior<sup>2)</sup>, Clovis Sperb de Barcellos<sup>3)</sup>**

1) Centro Universitário Newton Paiva, Coordenações das Engenharias, Rua José Cláudio Rezende, 420 – Estoril, CEP 30455-590, Belo Horizonte, M.G., Brasil (crisamagalhaes@hotmail.com)

2) Pontifícia Universidade Católica de Minas Gerais, Departamento de Engenharia Mecânica, Av. Dom Jose Gaspar, 500 – Coração Eucarístico, CEP 30535-901, Belo Horizonte, M.G., Brasil (✉ pamerico@pucminas.br, +55 31 9951 3121)

3) Universidade Federal de Santa Catarina, Departamento de Engenharia Mecânica, Campus Universitário Reitor João David Ferreira Lima – Trindade – Florianópolis – S.C., Brasil (clovis.barcellos@gmail.com)

### **Abstract**

Digital photoelasticity is an important optical metrology follow-up for stress and strain analysis using full-field digital photographic images. Advances in digital image processing, data acquisition, procedures for pattern recognition and storage capacity enable the use of the computer-aided technique in automation and facilitate improvement of the digital photoelastic technique. The objective of this research is to find new equations for a novel phase-shifting method in digital photoelasticity. Some innovations are proposed. In terms of phase-shifting, only the analyzer is rotated, and the other equations are deduced by applying a new numerical technique instead of the usual algebraic techniques. This approach can be used to calculate a larger sequence of images. Each image represents a pattern and a measurement of the stresses present in the object. A decrease in the mean errors was obtained by increasing the number of observations. A reduction in the difference between the theoretical and experimental values of stresses was obtained by increasing the number of images in the equations for calculating phase. Every photographic image has errors and random noise, but the uncertainties due to these effects can be reduced with a larger number of observations. The proposed method with many images and high accuracy is a good alternative to the photoelastic techniques.

Keywords: photoelasticity, metrology, stress analysis, strain measurement, optical measurement systems, optical interferometry, experimental techniques.

© 2013 Polish Academy of Sciences. All rights reserved

### **1. Introduction**

Photoelasticity is one of the oldest methods for experimental stress analysis, but it has been overshadowed by the Finite Element Method for engineering applications over the past two to three decades. However, certain new and novel developments and applications have revived the use of photoelasticity. The new approach involves the use of hybrid methods in which the advantages of both experimental and numerical methods are exploited. Nevertheless, recent industrial needs, such as continuous on-line monitoring of structures, determination of the residual stresses in glass (plastics) and microelectronics materials, rapid prototype production and dynamic visualization of stress waves, have brought photoelasticity into the limelight once again [1].

The current trend of digitally imaging photoelastic fringe patterns indicates that image processing can be used to delineate the required information from the fringe patterns. The phase-shifting method has the most potential, particularly with respect to fringe sign determination. The method of photoelasticity makes it possible to obtain the principal stress

directions and principal stress differences in a model. The principal stress directions and the principal stress differences are provided by isoclinics and isochromatics, respectively [2]. Isoclinics are the loci of the points in the specimen along which the principal stresses lie in the same direction. Isochromatics are the loci of the points along which the difference in the first and second principal stress remains the same. Thus, they are the lines that join the points with equal maximum shear stress magnitudes [3].

The fringe patterns are nothing but the record of the phase difference between light travelling in two different optical paths as intensity variations. By varying the phase difference between the beams involved, in known steps, it is possible to generate a sufficient number of equations to solve the parameters involved. In general, phase differences can be added by altering the optical path length of any one of the light beams. Usually, the phase of the reference light beam is altered in known steps. Photoelasticity falls into a special category, in that the two light beams cannot be treated separately, but rather always go together [4]. This means a phase shift introduced in one light beam will also introduce a corresponding phase shift in the other beam. This change in phase, in practice, is achieved by appropriately rotating the optical elements of the polariscope. A detailed study of the intensity of the light transmitted can help in relating the rotation of the optical elements to the change in phase introduced [5].

The significant advantage of the methodology proposed in this paper is that the method only changes the angle of the analyzer in the polariscope and that one can obtain equations for calculating the phase for any number of images in various situations. A clearer physical reason for the proposed numerical model is that the measurement uncertainty can be reduced by increasing the number of observations. Measurement uncertainty is a parameter characterizing the dispersion of the values attributed to a measured quantity. No measurement is exact. The uncertainty has a probabilistic basis and reflects incomplete knowledge of the quantity. All measurements are subject to uncertainty and a measured value is only complete if it is accompanied by a statement of the associated uncertainty. The new method can be used with any number of photographic images or photoelastic measures in a plane or circular polariscope [6].

## 2. Phase-shifting methods of analysis

The optical arrangement to recognize and to identify isoclinics and isochromatics from photoelastic fringes is a circular polariscope set-up, shown in Fig. 1. In Fig. 1,  $P$ ,  $Q$ ,  $R$ , and  $A$  represent the polarizer, quarter-wave plate, retarder (stressed model) and analyzer, respectively. The orientation of the element is written by a subscript, which means the angle between the polarizing axis and the horizontal  $x$  axis.  $R_{\alpha,\delta}$  represents the stressed sample taken as a retardation  $\delta$  and whose fast axis is at an angle  $\alpha$  with the  $x$  axis [7]. Therefore,  $P_{90}Q_{45}R_{\alpha,\delta}Q_{-45}A_{\theta}$  indicates the following: a polarizer at  $90^\circ$ , a quarter-wave plate with a fast axis at  $45^\circ$ , a specimen as retardation  $\delta$  whose fast axis is at an angle  $\alpha$  with the  $x$  axis, a quarter-wave plate with a fast axis at  $-45^\circ$ , and an analyzer at  $\theta$ . With the Jones calculus [8] for the arrangement of  $P_{90}Q_{45}R_{\alpha,\delta}Q_{-45}A_{\theta}$  shown in Fig. 1, the components of the electric field in light along and perpendicular to the analyzer axis ( $E_x, E_y$ ) are given as:

$$\begin{pmatrix} E_x \\ E_y \end{pmatrix} = \begin{bmatrix} \cos^2 \theta & \sin \theta \cos \theta \\ \sin \theta \cos \theta & \sin^2 \theta \end{bmatrix} \times \begin{bmatrix} 1+i & 1-i \\ 1-i & 1+i \end{bmatrix} \times \begin{bmatrix} e^{i\delta} \cos^2 \alpha + \sin^2 \alpha & (e^{i\delta} - 1) \sin \alpha \cos \alpha \\ (e^{i\delta} - 1) \sin \alpha \cos \alpha & e^{i\delta} \sin^2 \alpha + \cos^2 \alpha \end{bmatrix} \times \begin{pmatrix} i+1 \\ i \end{pmatrix} \begin{bmatrix} 1 & i \\ i & 1 \end{bmatrix} \begin{pmatrix} 0 \\ 1 \end{pmatrix} k e^{i\omega t}. \quad (1)$$

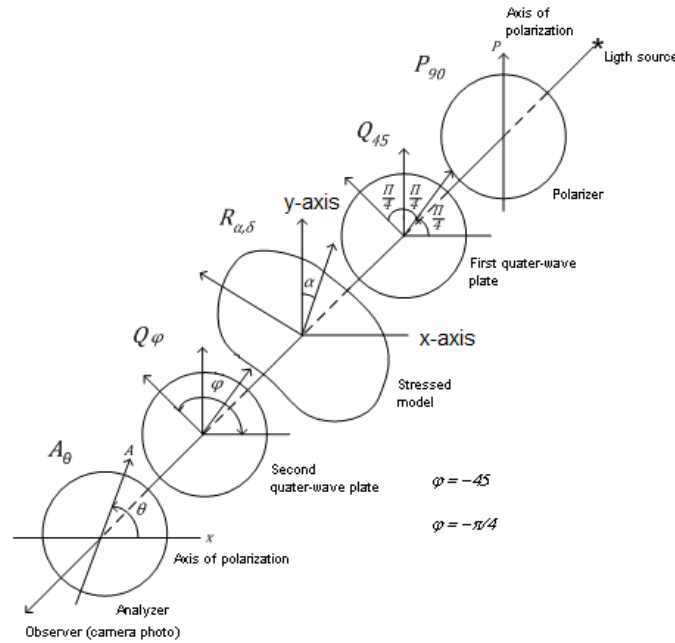


Fig. 1. Optical arrangement of a circular polariscope ( $180^\circ = \pi$  radians). In the figure we have a coordinate system where the x axis is horizontal and the vertical is the y-axis.

The angles  $\theta$  and  $\varphi = -45^\circ$  are those that the analyzer and the second quarter-wave plate form with the reference x axis, respectively. The symbols  $k$  and  $\omega$  are the amplitude and the angular frequency of the light vector, respectively.

$$I = E_x^* E_x + E_y^* E_y. \tag{2}$$

In (2),  $I$  is the output light intensity, and  $E_x^*$  and  $E_y^*$  are the complex conjugates of  $E_x$  and  $E_y$ , respectively. After the simple operation of (1) by (2), the output intensity of the circular polariscope for the arrangement  $P_{90}Q_{45}R_{\alpha,\delta}Q_{-45}A_\theta$  is given by:

$$I = K [1 - \cos(2\theta)\cos(\delta) - \cos(2\alpha)\sin(2\theta)\sin(\delta)], \tag{3}$$

where  $K$  is a proportional constant, *i.e.*, the maximum light intensity emerging from the analyzer. These angle values are chosen to simplify the calibration of the polariscope used in the experimental measurements. For the phase measuring technique, the angle  $\alpha$  and the relative retardation  $\delta$  indicating the direction and the difference of principal stresses, respectively, are the parameters to be obtained.

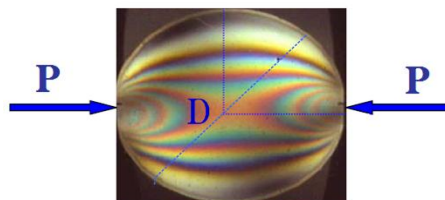


Fig. 2. Sample under compression.

In the experiments, Fig. 2, the diameter and the thickness of the disk used are:  $D = 10.0$  cm and  $H = 0.5$  cm, respectively. A diametrical compression load,  $P = 50.0$  N, is applied to the disk. The material fringe constant  $F = 900.00$  N/m is used. From the given conditions, the theoretical value of isochromatic  $\delta$  is related to two principal stress components,  $\sigma_1$  and  $\sigma_2$ ,

as in (4). In contrast, the theoretical isocline angle  $\alpha$  can be calculated by (4) using stress components  $\sigma_x$ ,  $\sigma_y$ , and  $\tau_{xy}$ .

$$\delta = \frac{2\pi H}{F}(\sigma_1 - \sigma_2) \quad \alpha = \frac{1}{2} \tan^{-1} \left( \frac{2\tau_{xy}}{\sigma_x - \sigma_y} \right). \quad (4)$$

In the literature on the theory of elasticity [9–10], the exact value of the stress field, as a function of  $x$  and  $y$  with its origin at the center of the disc, is given by (the superscript “ $e$ ” indicates the exact, analytical values):

$$\sigma_x^e = \frac{-2P}{\pi H} \left\{ \frac{(D/2 - y)x^2}{[x^2 + (D/2 - y)^2]^2} + \frac{(D/2 + y)x^2}{[x^2 + (D/2 + y)^2]^2} - \frac{1}{D} \right\}, \quad (5)$$

$$\sigma_y^e = \frac{-2P}{\pi H} \left\{ \frac{(D/2 - y)^3}{[x^2 + (D/2 - y)^2]^2} + \frac{(D/2 + y)^3}{[x^2 + (D/2 + y)^2]^2} - \frac{1}{D} \right\}, \quad (6)$$

$$\tau_{xy}^e = \frac{2P}{\pi H} \left\{ \frac{(D/2 - y)^2 x}{[x^2 + (D/2 - y)^2]^2} + \frac{(D/2 + y)^2 x}{[x^2 + (D/2 + y)^2]^2} \right\}. \quad (7)$$

For comparison with the experimentally measured values, the following are used:

$$\sigma_1^e = \frac{(\sigma_x^e + \sigma_y^e)}{2} - \sqrt{\frac{1}{4}(\sigma_x^e - \sigma_y^e)^2 + (\tau_{xy}^e)^2} \quad \sigma_2^e = \frac{(\sigma_x^e + \sigma_y^e)}{2} + \sqrt{\frac{1}{4}(\sigma_x^e - \sigma_y^e)^2 + (\tau_{xy}^e)^2}. \quad (8)$$

Then, with (9), the exact values of  $\delta^e$  and  $\alpha^e$  can be calculated for each point of the  $x$  and  $y$  coordinates in the same manner as in (4):

$$\delta^e = \frac{2\pi H}{F}(\sigma_1^e - \sigma_2^e) \quad \alpha^e = \frac{1}{2} \tan^{-1} \left( \frac{2\tau_{xy}^e}{\sigma_x^e - \sigma_y^e} \right). \quad (9)$$

The idea is to compare these exact results ( $\delta^e$  and  $\alpha^e$ ) obtained theoretically in the analysis of stress with experimental measurements of light intensities using the proposed method ( $\delta$  and  $\alpha$ ).

### 3. New mathematical model

By analogy with the equations of phase calculation used by other authors and the mathematical model proposed in [11], we had the idea to try a new general model for the equations of phase in photoelasticity. After many different attempts, a general equation for calculating the phase for any number,  $N$ , of images is proposed:

$$\alpha = \frac{1}{2} \tan^{-1} \left( \frac{\sqrt{\sum_{r=1}^N \sum_{s=r}^N b_{r,s} I_r I_s}}{\sqrt{\sum_{r=1}^N \sum_{s=r}^N c_{r,s} I_r I_s}} \right) \quad \delta = \tan^{-1} \left( \frac{\sqrt{\sum_{r=1}^N \sum_{s=r}^N e_{r,s} I_r I_s}}{\sqrt{\sum_{r=1}^N \sum_{s=r}^N f_{r,s} I_r I_s}} \right), \quad (10)$$

where  $N$  is the number of images,  $b_{r,s}$  and  $e_{r,s}$  are coefficients of the numerator,  $c_{r,s}$  and  $f_{r,s}$  are coefficients of the denominator, and  $r$  and  $s$  are the indices of the sum [11].

The use of the absolute value in the numerator and the denominator restricts the angle between 0 and  $\pi/2$  radians but avoids negative roots and also eliminates false angles. Subsequent considerations will later remove this restriction.

The shift from obtaining equations for calculating the phase analytically to obtaining them numerically is a significant innovation. It breaks a paradigm that was hitherto used by several authors. After several attempts at numerical modeling of the problem, the following mathematical problem was identified (11):

$$\begin{aligned} & \text{Maximize} \quad \sum_{r=1}^N \sum_{s=r}^N (b_{r,s} + c_{r,s} + e_{r,s} + f_{r,s}) \\ & \text{subject to} \end{aligned}$$

$$\left\{ \begin{array}{ll} \tan(\text{angle}) = \text{Sqrt}(|\text{Num}|)/\text{Sqrt}(|\text{Den}|) & \text{Quantities} \\ 1) \quad \tan^2(2\alpha^v) \left( \sum_{r=1}^N \sum_{s=r}^N (c_{r,s} I_r^v I_s^v) \right) = \sum_{r=1}^N \sum_{s=r}^N (b_{r,s} I_r^v I_s^v) & v = 1..[N(N+1)] \\ 2) \quad \tan^2(\delta^v) \left( \sum_{r=1}^N \sum_{s=r}^N (f_{r,s} I_r^v I_s^v) \right) = \sum_{r=1}^N \sum_{s=r}^N (e_{r,s} I_r^v I_s^v) & v = 1..[N(N+1)] \\ 3) \quad \begin{array}{ll} -1 \leq b_{r,s} \leq 1, & -1 \leq c_{r,s} \leq 1 \\ -1 \leq e_{r,s} \leq 1, & -1 \leq f_{r,s} \leq 1 \end{array} & r = 1..N, s = r..N \\ 4) \quad \begin{array}{ll} b_{r,s}, c_{r,s} \text{ are real numbers} & r = 1..N, s = r..N \\ e_{r,s}, f_{r,s} \text{ are real numbers} & r = 1..N, s = r..N \end{array} \end{array} \right.$$

where for each  $v$ :

$$\left\{ \begin{array}{l} I_j^v = K^v \left[ 1 - \cos(2\theta_j) \cos(\delta^v) - \cos(2\alpha^v) \sin(2\theta_j) \sin(\delta^v) \right], j = 1..N \\ K^v \in [0; 255] \text{ random and real} \\ \alpha^v \in [0; \pi/4] \text{ random and real} \\ \delta^v \in [0; \pi/2] \text{ random and real} \\ \theta_j = \frac{\pi}{2} \left( \frac{j-1}{\text{Step}-1} \right) - \frac{\pi}{4}, j = 1..N, \quad \theta_j \in \left[ -\pi/4, \pi/4 \right] \\ \Delta\theta = \frac{\pi}{2(\text{Step}-1)} \text{ radians} \end{array} \right. \quad (11)$$

Input with the integer values:  $\text{Step} \geq 3$  and  $N \in [3, \text{Step}]$

Output with the real coefficients:  $b_{r,s}, c_{r,s}, e_{r,s}, f_{r,s}, r = 1..N, s = r..N$

The motivation for choosing this mathematical model is the success achieved in [11] with a similar model. The idea of the mathematical model is to maximize the coefficients ( $b_{r,s}, c_{r,s}, e_{r,s}, f_{r,s}$ ) so that their values are large enough (not close to zero) to make them significant in the equation obtained. *Step* represents integer values greater than or equal to 3. *N* is the number of images, and it is an integer number between 3 and the value of *Step*.

The constraints 1 and 2 are made so that the coefficients ( $b_{r,s}, c_{r,s}, e_{r,s}, f_{r,s}$ ) generate correct values for the calculation of  $\alpha$  and  $\delta$ . To ensure that one has a hyperrestricted problem, it is suggested that the number of greater restrictions must be at least equal to the number of variables. The constraints 3 and 4 are placed on the coefficients ( $b_{r,s}, c_{r,s}, e_{r,s}, f_{r,s}$ ) that are not

greater than one and are not smaller than minus one, to avoid error propagation. For the needs of phase evaluation, these limiting factors will increase the values of the intensity of the observations ( $I$ ) that contains errors due to noise in the observations and excellent discretization in pixels and in shades of gray.

The  $\nu$  restrictions in the model are obtained by a random choice of values for  $K$  (constant proportion of the maximum intensity of light emerging from the analyzer),  $\delta$  (delay in the model given by the photoelastic isochromatic fringes) and  $\alpha$  (angle between the direction and the axis of horizontal reference  $\sigma_1$ ). In fact, the values of  $K$ ,  $\delta$ , and  $\alpha$  can be any real number, but to maintain compatibility with the problem, we chose to limit  $K$  between 0 and 255 so that the values of  $I$  are between 0 and 255. In addition,  $\alpha$  is limited between 0 and  $\pi/4$  radians and  $\delta$  between 0 and  $\pi/2$  radians so that the tangents have positive values.

The angle  $\theta$  is limited to  $-\pi/4$  and  $\pi/4$  radians and is equally spaced when  $Step = N$ . For other values of  $Step$ , the angle  $\theta$  starts with a value of  $-\pi/4$  and is equally spaced, but it does not reach  $\pi/4$ . The choice of these angles is based on the ease of calibration in the polariscope used. Other values for the angles can be used in the mathematical model.

$Step$  must to be an integer number. The number of images ( $N$ ) should range from 3 to the value of  $Step$ .  $Step$  is used to vary the angle with constant spacing in the polariscope analyzer. For example, for 8 images ( $N = 8$ ) and  $Step=10$ , the angles of the analyzer polariscope ( $\theta$ ) are as follows:  $-45^\circ, -35^\circ, -25^\circ, -15^\circ, -5^\circ, 5^\circ, 15^\circ$ , and  $25^\circ$ .

The mathematical model is easy to solve because it involves linear programming and a maximum global solution can be obtained using the Simplex method. The processing time for the solution of this mathematical model is very fast, a few seconds on personal computers.

For example, when  $N = 3$  and  $Step = 3$ , the angles of the polariscope analyzer ( $\theta$ ) are  $-45^\circ, 0^\circ$ , and  $45^\circ$ . The equations obtained with the mathematical model are shown in (12).

$$\alpha = \frac{1}{2} \tan^{-1} \left( \frac{\sqrt{\begin{matrix} -0.25I_1^2 & + I_1I_2 & + 0.5I_1I_3 \\ & -I_2^2 & + I_2I_3 \\ & & -0.25I_3^2 \end{matrix}}}{\sqrt{\begin{matrix} 0.25I_1^2 & & -0.5I_1I_3 \\ & & + 0.25I_3^2 \end{matrix}}} \right) \quad \delta = \tan^{-1} \left( \frac{\sqrt{\begin{matrix} I_1I_2 \\ -I_2^2 & + I_2I_3 \end{matrix}}}{\sqrt{\begin{matrix} 0.25I_1^2 & -I_1I_2 & + 0.5I_1I_3 \\ & + I_2^2 & -I_2I_3 \\ & & + 0.25I_3^2 \end{matrix}}} \right). \quad (12)$$

In another different example, when  $N = 6$  and  $Step = 6$ , the angles of the polariscope analyzer ( $\theta$ ) are  $-45^\circ, -27^\circ, -9^\circ, 9^\circ, 27^\circ$ , and  $45^\circ$ . Here the differences are in coefficients be integers instead of real, this was done by changing the mathematical model for integer programming. The equations obtained with the mathematical model are shown in (13).

$$\alpha = \frac{1}{2} \tan^{-1} \left( \frac{\sqrt{\begin{matrix} -2I_1^2 & + 2I_1I_2 & + 2I_1I_3 & + 2I_1I_4 & + 2I_1I_5 & + I_1I_6 \\ & -I_2^2 & & & -2I_2I_5 & + 2I_2I_6 \\ & & -I_3^2 & -2I_3I_4 & & + 2I_3I_6 \\ & & & -I_4^2 & & + 2I_4I_6 \\ & & & & -I_5^2 & + 2I_5I_6 \\ & & & & & -2I_6^2 \end{matrix}}}{\sqrt{\begin{matrix} I_1^2 & + 2I_1I_2 & -I_1I_3 & + I_1I_4 & -2I_1I_5 & -2I_1I_6 \\ & -I_2^2 & -2I_2I_3 & + 2I_2I_4 & + 2I_2I_5 & -2I_2I_6 \\ & & + I_3^2 & -2I_3I_4 & + 2I_3I_5 & + I_3I_6 \\ & & & + I_4^2 & -2I_4I_5 & -I_4I_6 \\ & & & & -I_5^2 & + 2I_5I_6 \\ & & & & & + I_6^2 \end{matrix}}} \right) \quad \delta = \tan^{-1} \left( \frac{\sqrt{\begin{matrix} 2I_1I_2 & + 2I_1I_3 & + 2I_1I_4 & + 2I_1I_5 & -3I_1I_6 \\ -2I_2^2 & & & & + 2I_2I_6 \\ & -2I_3^2 & & & + 2I_3I_6 \\ & & -2I_4^2 & & + 2I_4I_6 \\ & & & -2I_5^2 & + 2I_5I_6 \end{matrix}}}{\sqrt{\begin{matrix} 2I_1^2 & -2I_1I_2 & -2I_1I_3 & -2I_1I_4 & -2I_1I_5 & + 4I_1I_6 \\ & + I_2^2 & & & + 2I_2I_5 & -2I_2I_6 \\ & & + I_3^2 & + 2I_3I_4 & & -2I_3I_6 \\ & & & + I_4^2 & & -2I_4I_6 \\ & & & & + I_5^2 & -2I_5I_6 \\ & & & & & + 2I_6^2 \end{matrix}}} \right) \quad (13)$$

Thus, for each value of *Step* greater than or equal to 3 and *N* between 3 and the value of *Step*, the mathematical model (11) provides values of the real coefficients ( $b_{r,s}$ ,  $c_{r,s}$ ,  $e_{r,s}$ ,  $f_{r,s}$ ), which represents an unprecedented and new phase equation for  $\alpha$  and  $\delta$ .

Because the new equations were developed from the algorithms, a numerical calculation, rather than an analytical demonstration of trigonometric relations, is necessary to check them. It is believed that a large number of numerical tests can validate or verify these new equations or at least minimize the chance of these equations being wrong or false. To test the usefulness of the new equations for calculating the phase, a computer program was created that generated random values of  $K \in [0, 255]$ ,  $\alpha' \in [0, \pi/4]$ , and  $\delta' \in [0, \pi/2]$ . Using (3), the program calculates *N* values of  $I_j$ , one for each value of  $\theta_j$ . With the values of  $I_j$ , the new phase equations were applied and tested to determine whether they produced the correct values of  $\alpha$  and  $\delta$ . The values of  $I_j$  (luminous intensity of the image) are calculated with *j* ranging from 1 to *N*. The new equations with the values of  $I_j$  are applied, giving a  $\tan(\alpha)$  and a  $\tan(\delta)$  that must be compared with the value of randomly assigned ( $\alpha'$  and  $\delta'$ ) values. This comparison involves the accuracy of a very small value because of the number of rounding errors that can occur in the calculations, that is, the precision  $(|\alpha' - \alpha| + |\delta' - \delta|) \leq 10^{-6}$ . This calculation was performed thousands of times (at least 100.000 times) for each equation in the phase calculation. It was generated in at least 99.999% of the time with an accuracy of  $10^{-6}$ . The mathematical model of (11) was successfully tested until *Step* and *N* equal 1801, the value at which the increment  $\Delta\theta$  would be  $0.05^\circ$ . Thus, it was believed that the chances for the equations to be wrong or false have been minimized.

#### 4. Before unwrapping, change to $[-\pi, \pi]$

Because of the character of the evaluation equations, only phase values  $\alpha \in [0, \pi/4]$  and  $\delta \in [0, \pi/2]$  radians were calculated. For unequivocal determination of the wrapped phase value angles  $\in [-\pi, \pi]$  it was necessary to test values  $\delta$ ,  $-\delta$ ,  $\delta - \pi$ , and  $-\delta + \pi$  by combining them with  $\alpha$ ,  $-\alpha$ ,  $\alpha - \pi$ , and  $-\alpha + \pi$  using values of  $I_j$  and small systems in (14):

$$\begin{cases} I_1 = K[1 - \cos(2\theta_1)\cos(\delta) - \cos(2\alpha)\sin(2\theta_1)\sin(\delta)] \\ I_2 = K[1 - \cos(2\theta_2)\cos(\delta) - \cos(2\alpha)\sin(2\theta_2)\sin(\delta)] \\ \dots \\ I_N = K[1 - \cos(2\theta_N)\cos(\delta) - \cos(2\alpha)\sin(2\theta_N)\sin(\delta)] \end{cases} \quad (14)$$

The values were tested based on the symmetries of the tangent function. Sixteen tests are performed, and the correct values of  $\alpha$  and  $\delta$  are sought between  $-\pi$  and  $\pi$  because the experimental values  $I_j$  and  $\theta_j$  are known [12].

We obtain  $\alpha$  and  $\delta$  between  $[-\pi, \pi]$ . The next step is to unwrap the phase map. When unwrapping, several of the phase values should be shifted by an integer multiple of  $2\pi$ . Unwrapping is thus adding or subtracting  $2\pi$  offsets at each discontinuity encountered in the phase data. The unwrapping procedure consists of finding the correct field number for each phase measurement [13–14].

Once obtained the value of  $\alpha$  and  $\delta$  unwrapping, applies digital implementation of the shear difference technique for whole field stress separation of 2-D problems of any geometry shown in [15–17]. Thus, it calculates the values of the phase maps, principal tensions ( $\sigma_1$ ,  $\sigma_2$ ) and normal ( $\sigma_x$ ,  $\sigma_y$ ) and shear ( $\tau_{xy}$ ) stresses. The von Mises stress or equivalent tensile stress ( $\sigma_v$ ), a scalar stress value that can be computed, too. Thereafter, graphical displays of tensions in the object under study are shown.

## 5. Testing and analysis of error

To assess the practical use of the method developed in this work, a stress disk under diametric compression,  $D = 100.0$  mm in diameter,  $H = 5.0$  mm thick and made of epoxy, is used. The pixel numbers, which are used for digitization, are  $1024 \times 1024$ . The grey level of each pixel ranges from 0 to 255. The light source used in this experiment is white light from a sodium lamp.

To test the new equations for the phase calculation, they were used with the technique of photoelasticity for an object with known stress and to evaluate the average error using (15):

$$\text{Average Error for } \alpha \ (E_\alpha) = \frac{1}{M} \sum_{i=1}^M |\alpha_i^e - \alpha_i|, \text{ Average Error for } \delta \ (E_\delta) = \frac{1}{M} \sum_{i=1}^M |\delta_i^e - \delta_i|, \quad (15)$$

where  $M$  is the number of pixels of the image and  $\alpha_i^e$  and  $\delta_i^e$  are the exact value calculated by (6–12) for the disk. The values of  $\alpha_i$  and  $\delta_i$  are calculated by the new equation. In the analysis of the error, only the zones within the photos that were unambiguous and contained no inconsistencies were considered [18–20]. Fig. 4 show the results obtained with the application of the new phase calculation equations.

This process was started with three images, repeated with four, then five and so on. The idea was to show that with an increasing number of images, the average error tends to decrease. Fig. 3 shows an example of this procedure.

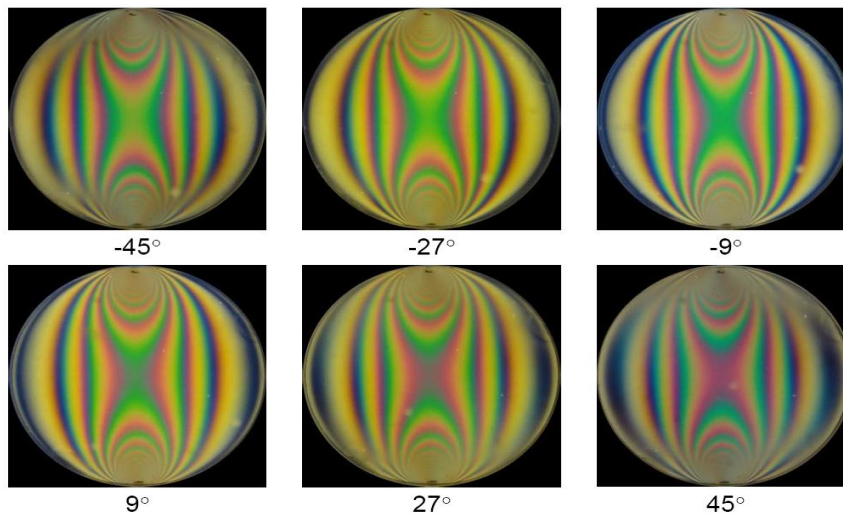


Fig. 3. Set with 6 images,  $\Delta\theta$  equal to  $18^\circ$ , the disk is under compression.

To compare the new equations for calculating the phase, nine sets of photos with *Step* set to 3, 4, 6, 7, 10, 11, 16, 19, and 31 were generated. In each set, the angle  $\theta$  of the analyzer is varied ( $\Delta\theta$ ):  $45^\circ$ ,  $30^\circ$ ,  $18^\circ$ ,  $15^\circ$ ,  $10^\circ$ ,  $9^\circ$ ,  $6^\circ$ ,  $5^\circ$ , and  $3^\circ$ , respectively. Each set was computed using the average error of 3 to the number of *Step* images and using equations to evaluate the angles  $\alpha$  and  $\delta$ . Fig. 5 and Fig. 6 show that the average error decreases when the number of images increases. It may be noted that for a number of images, the average error increases when the variation of the angle  $\theta$  between the images decreases.

It is important to note that for each equation developed, the average errors found for the angle  $\delta$  are larger than the errors found for the angle  $\alpha$  of the fringes isoclines. It is believed that this occurs because the absolute values of  $\delta$  are higher than the absolute values of  $\alpha$ .



To compare the equations with the equations deduced by other authors, the equations were applied to the analysis of error in the algorithm of Patterson and Wang [21]. Values of  $E_\alpha = 2104 \times 10^{-6}$  rad and  $E_\delta = 5312 \times 10^{-6}$  rad were obtained.

For the Patterson and Wang algorithm with six images, the average error is less than six images using the new equations. It is believed that the major distinction between the pictures of the phase shifts is the reason why this improved result is obtained. However, to obtain these images, it is necessary to rotate the analyzer and the second plate of the polariscope by a quarter wave.

The average error of the algorithm of Wang and Patterson with 6 images is in the range of the average error found for 11 images using the new equations, but for more than 16 images, lower average errors for the newly developed equations can be observed, indicating that a larger number of images yielded smaller errors. Similar results were obtained with the algorithms proposed by other authors in [22–26].

More experiments were performed with other values of load ( $P$ ), diameter of the disk ( $D$ ), the disk thickness ( $H$ ), and material fringe constant ( $F$ ) with very similar results. These new experiments were conducted to validate and confirm the proposed method.

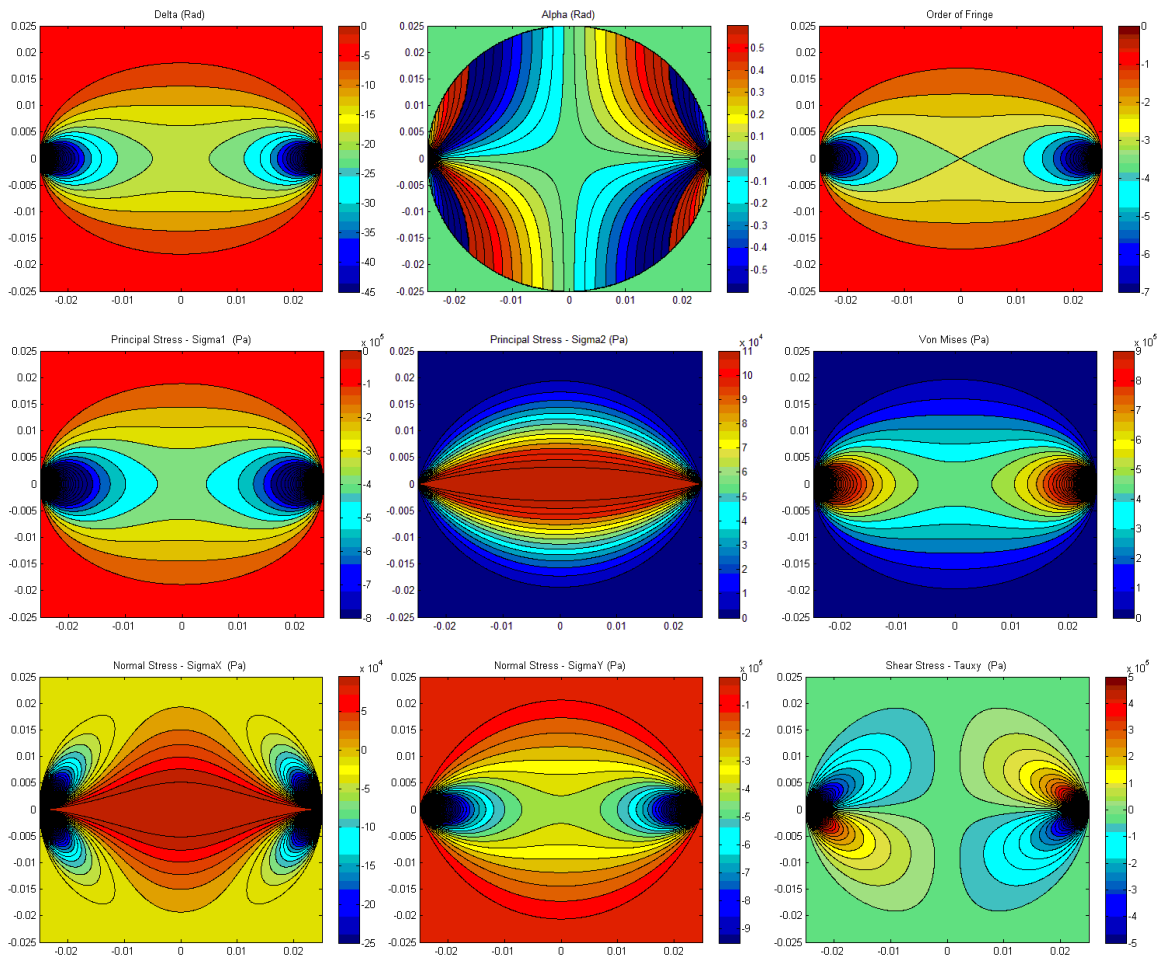


Fig. 4: Results obtained through experimental measurements using the new equations with  $N = 19$  and  $Step = 10$  of:  $\delta$ ,  $\alpha$ , fringe order( $n$ ),  $\sigma_1$ ,  $\sigma_2$ , von Mises stress( $\sigma_v$ ),  $\sigma_x$ ,  $\sigma_y$  and  $\tau_{xy}$ .

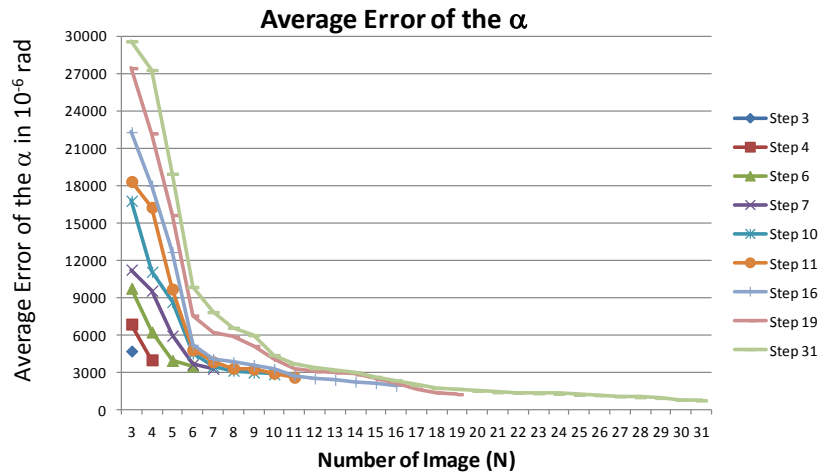


Fig. 5. A plot of the average error in  $10^{-6}$  rad versus the number of frames ( $N$ ) for angle  $\alpha$ .

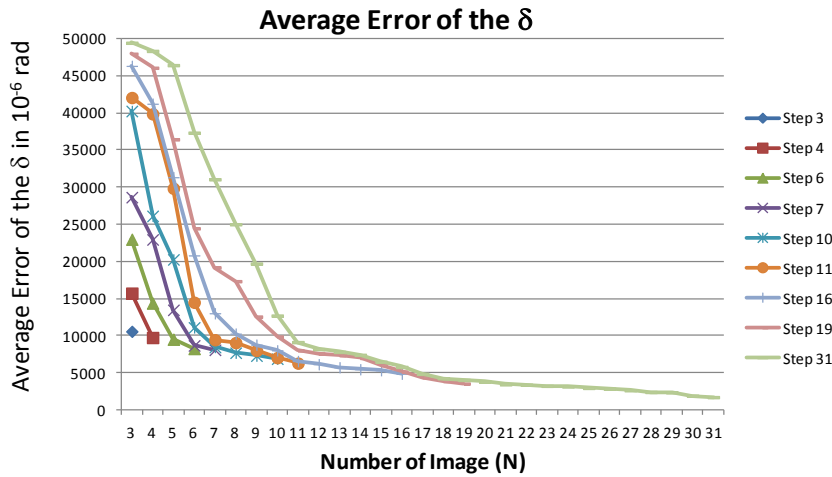


Fig. 6. A plot of the average error in  $10^{-6}$  rad versus the number of frames ( $N$ ) for angle  $\delta$ .

## 6. Conclusion

This paper addresses the equations used for phase calculation measurements with images using the phase shifting technique. New equations are shown to be capable of processing the optical signal of photoelasticity. These techniques are very precise, easy to use and of low cost. On the basis of the performed error analysis, it can be concluded that the new equations are very good phase calculation algorithms. The metric analysis of the considered system demonstrated that its uncertainties of measurement depend on the frame period of the grid, on the resolution of photos in pixel and on the number of frames. However, the uncertainties involved in the measurement of the geometric parameters and the phase still require attention. In theory, if we have many frames, the measurement errors become very small. The measurement results obtained by the optical system demonstrate its industrial and engineering applications in experimental mechanics.

New numerical equations are deduced to calculate the directions of the tensions and delays (phase maps of the isoclines and isochromatic fringes) for the full-field image automatically, by programming the phase shift method in digital photoelasticity. With these new equations, a larger number of images phase shifted only by rotation of the analyzer can be used, and the gain can be calculated with lower uncertainties. Numerical methods were employed in an unprecedented way with the photoelastic technique to obtain a methodology for deriving the

new equations. Until now, these equations were determined by algebraic and analytic methods.

With the new equations, it was possible to develop a photoelastic system that moves the analyzer of the polariscope at a constant speed while a camera takes many pictures at equal intervals of times, like a film. The camera must have a very short exposure time (high shutter speeds). With this technique, the obtained measurements are more precise, and there are fewer uncertainties.

Digital photoelasticity is an important optical metrology follow-up for stress and strain analysis using full-field digital photographic images. Advances in digital image processing, data acquisition, procedures for pattern recognition and storage capacity enable use of the computer-aided technique in automation and facilitate improvement of the digital photoelastic technique. Photoelasticity has seen some renewed interest in the past few years with digital imaging, image processing and new methods becoming readily available. However, further research is needed to improve the accuracy, the precision and the automation of the photoelastic technique.

## Acknowledgments

The authors thank the generous support of the Pontificia Universidade Catolica de Minas Gerais – PUCMINAS, the Conselho Nacional de Desenvolvimento Cientifico e Tecnológico – CNPq – “National Council of Technological and Scientific Development” and Fundacao de Amparo a Pesquisa de Minas Gerais – FAPEMIG – “Foundation for Research Support of Minas Gerais”.

## References

- [1] Asundi, A.K. (2002). *MATLAB for Photomechanics – A Primer*. Elsevier Science.
- [2] Asundi, A.K., Tong, T., Boay, C.G. (2000). Determination of isoclinic and isochromatic parameters using the three-load method. *Meas. Sci. Technol.*, 11, 532, DOI:10.1088/0957-0233/11/5/313.
- [3] Ramesh, K. (2000). Digital Photoelasticity. *Meas. Sci. Technol.*, 11, 1826, DOI:10.1088/0957-0233/11/12/704.
- [4] Konwerska-Hrabowska, J. (1999). Optical pressure sensors using the spectral photoelastic effect. *Metrologia*, 36, 591, DOI:10.1088/0026-1394/36/6/21.
- [5] Yoneyama, S, Kamihoriuchi, H. (2009). A method for evaluating full-field stress components from a single image in interferometric photoelasticity. *Meas. Sci. Technol.*, 20, 075302, DOI:10.1088/0957-0233/20/7/075302.
- [6] Chernozatonski, L.A., Gramotnev, D.K., Vakulenko, A.V. (1990). Geometrical mechanism of photoelastic interaction in superlattices. *Physics Letters A*, 144(2), 105–110.
- [7] Baek, T.H., Kim, M.S., Morimoto, Y., Fujigaki, M. (2002). Separation of isochromatics and isoclinics from photoelastic fringes in a circular disk by phase measuring technique. *KSME International Journal*, 16(2), 175–181.
- [8] Collett, E. (2005). *Field Guide to Polarization*. SPIE Publications, FG05.
- [9] Ng, T.W. (1997). Derivation of retardation phase in computer-aided photoelasticity by using carrier fringe phase shifting. *Appl. Opt.*, 36, 8259–8263.
- [10] Oh, J.T., Kim, S.W. (2003). Polarization-sensitive optical coherence tomography for photoelasticity testing of glass/epoxy composites. *Opt. Express*, 11, 1669–1676.
- [11] Magalhaes Jr, P.A.A., Neto, P.S., Magalhães, C.A. (2010). New Carré Equation. *Metrol. Meas. Syst.*, 17(2), 173–194.

- [12] Toto-Arellano, N.I., Rodriguez-Zurita, G., Meneses-Fabian, C., Vazquez-Castillo, J.F. (2008). Phase shifts in the Fourier spectra of phase gratings and phase grids: an application for one-shot phase-shifting interferometry. *Opt. Express*, 16, 19330–19341.
- [13] Estrada, J.C., Servin, M., Quiroga, J.A. (2011). Noise robust linear dynamic system for phase unwrapping and smoothing. *Opt. Express*, 19, 5126–5133.
- [14] Navarro, M.A., Estrada, J.C., Servin, M., Quiroga, J.A., Vargas, J. (2012). Fast two-dimensional simultaneous phase unwrapping and low-pass filtering. *Opt. Express*, 20, 2556–2561.
- [15] Ramji, M., Ramesh, K. (2008). Whole field evaluation of stress components in digital photoelasticity – issues, implementation and application. *Opt. Lasers. Eng.*, 46(3), 257–71.
- [16] Ramji, M., Ramesh, K. (2008). Stress separation in digital photoelasticity, Part A – photoelastic data unwrapping and smoothing. *J. Aerosp. Sci. Technol.*, 60(1), 5–15.
- [17] Ramji, M., Ramesh, K. (2008). Stress separation in digital photoelasticity, Part B – whole field evaluation of stress components. *J. Aerosp. Sci. Technol.*, 60(1), 16–25.
- [18] Pinit, P., Umezaki, E. (2007). Digitally whole-field analysis of isoclinic parameter in photoelasticity by four-step color phase shifting technique. *Optics and Laser in Engineering*, 45, 795–807.
- [19] Ashokan, K., Ramesh, K. (2009). Finite element simulation of isoclinic and isochromatic phasemaps for use in digital photoelasticity. *Experimental Techniques*, 33, 38–44.
- [20] Ramesh, K. (2000). *Digital photoelasticity: advanced techniques and applications*. Springer-Verlag, Berlin, Germany.
- [21] Patterson, E.A., Wang, Z.F. (1991). Towards full field automated photoelastic analysis of complex components. *Strain*, 27(2), 49–5.
- [22] Ramji, M., Prasath, R.G.R. (2011). Sensitivity of isoclinic data using various phase shifting techniques in digital photoelasticity towards generalized error sources. *Optics and Lasers in Engineering*, 49(9–10), 1153–1167.
- [23] Chang, S.H., Wu, H.H.P. (2011). Improvement of digital photoelasticity based on camera response function. *Appl. Opt.*, 50, 5263–5270.
- [24] Ajovalasit, A., Petrucci, G., Scafidi, M. (2012). RGB photoelasticity applied to the analysis of membrane residual stress in glass. *Meas. Sci. Technol.*, 23, 025601, DOI:10.1088/0957-0233/23/2/025601.
- [25] Buckberry, C., Towers, D. (1995). Automatic analysis of isochromatic and isoclinic fringes in photoelasticity using phase measuring techniques. *Meas. Sci. Technol.*, 6, 1227, DOI:10.1088/0957-0233/6/9/001.
- [26] Quiroga, J.A., González-Cano, A. (2000). Automatic determination of isostatics in two-dimensional photoelasticity. *Meas. Sci. Technol.*, 11, 259 DOI:10.1088/0957-0233/11/3/313.